Available online at www.sciencedirect.com
SCIENCE DIRECT
Journal of Power Sources 157 (2006) 335–350
JOURNAL OF POWER SOURCES
www.elsevier.com/locate/jpowsour

Yttrium, cobalt and yttrium/cobalt oxide coatings on ferritic stainless steels for SOFC interconnects

Wei Qu [a,1], Li Jian [b], Douglas G. Ivey [c,*], Josephine M. Hill [a,*]

[a] *Department of Chemical and Petroleum Engineering, University of Calgary, Calgary, Alta., Canada T2N 1N4*
[b] *School of Materials Science and Engineering, State Key Laboratory of Plastic Forming Simulation and Die & Mould Technology, Huazhong University of Science and Technology, Wuhan, Hubei 430074, PR China*
[c] *Department of Chemical and Materials Engineering, University of Alberta, Edmonton, Alta., Canada T6G 2G6*

Received 20 June 2005; accepted 23 July 2005
Available online 8 September 2005

Abstract

Ferritic stainless steels are being considered as potential interconnect materials for SOFCs, in part because of their low cost relative to alternatives. These materials are, however, susceptible to degradation over time. A primary source of degradation is an increase in the area specific resistance (ASR), which is due to the formation of poorly conducting oxides (Mn–Cr spinel and Cr_2O_3) on the surface. In this work, the influence of Y, Co and Y/Co oxide coatings on the oxidation behaviour of a ferritic stainless steel (16–18 wt% Cr) has been investigated. Samples were oxidized in air for up to 500 h at temperatures ranging from 700 to 800 °C. Coated and uncoated samples were characterized, before and after heat treatment, using X-ray diffraction (XRD), scanning electron microscopy (SEM), thermogravimetric (TG) analysis and four-point probe resistance measurements.

Surface morphology investigations of coated and uncoated stainless steels showed differences for Y and Co in terms of oxide formation. In all cases, Cr–Mn spinel and Cr_2O_3 were the two main surface oxides; however, the morphology of the spinel phase was dependent on the type of coating. The lowest resistances were obtained for the Y/Co-coated samples, which had ASR values up to seven times lower than corresponding uncoated ferritic stainless steels.

Keywords: Interconnects; Yttrium; Cobalt; Coatings; Solid-oxide fuel cells; Oxide formation

1. Introduction

Solid oxide fuel cells (SOFCs) are classified as intermediate temperature (650–800 °C) fuel cells. Individual planar SOFCs are connected in a stack with electronically conducting plates called interconnects. The desirable properties of interconnects include mechanical stability at the operating temperature, thermal and chemical compatibility with the electrode materials, low cost and ease of fabrication. On the anode side, interconnects are exposed to highly reducing conditions, while on the cathode side they are exposed to highly oxidizing conditions. The highly oxidizing environment is conducive to oxide growth that can reduce the conductivity of the interconnect.

Several factors are associated with oxide formation–oxide thickness, conductivity of the oxide and adherence of the oxide to the substrate. Based on these factors, different methods have been proposed to extend the lifetime of interconnect materials. Various alloy compositions have been studied [1–6], but the general consensus is that no single alloy can fully satisfy all the SOFC operating requirements and resist oxide formation. Recently, chromia-forming ferritic stainless steels, which have a thermal expansion coefficient close to that for the yttria-stabilized zirconia (YSZ) SOFC system,

* Corresponding authors. Tel.: +1 780 492 2957; fax: +1 780 492 2881.
E-mail addresses: doug.ivey@ualberta.ca (D.G. Ivey), jhill@ucalgary.ca (J.M. Hill).
[1] Present address: National Research Council, Institute for Fuel Cell innovations, Vancouver, BC, Canada V6T 1W5.

0378-7753/$ – see front matter © 2005 Elsevier B.V. All rights reserved.
doi:10.1016/j.jpowsour.2005.07.052

have become of interest to SOFC developers because of their relatively low cost and ease of manufacturing. These steels, however, form relatively thick chromia (Cr_2O_3) scales at high temperatures (>700 °C). Although this oxide scale protects the underlying metal from further exposure to the corroding gases [7], the scale has very poor electrical conductivity and, thus, increases the resistance of the system. In addition, if the scale does not adhere well to the substrate, additional oxide will form and the conductivity will decrease further.

One approach to improve the oxide growth resistance of stainless steel interconnects is to apply a coating that may reduce the rate of oxide formation as well as modify the properties of the oxide that is generated by the substrate. The specific results obtained depend on several factors including the composition of the stainless steel, the oxidation temperature, the oxidation time and the method used to apply the coating. In general, however, the addition of a small amount (<0.5 wt%) of a rare earth element, such as yttrium or lanthanum has been shown to significantly reduce oxide growth [8–10]. The beneficial effects of rare earth elements on the high temperature oxidation behaviour of nickel-, cobalt- and iron-based alloys have previously been attributed to the formation of perovskite compounds at oxide grain boundaries [1,11]. The ability of a rare earth element to decrease oxide formation depends on the nature of the rare earth element and its position within the lanthanide series. Yttria (Y_2O_3) has been shown to be the best of the rare earths studied, despite having the slowest reaction rate to form a perovskite phase [8,9]. Studies conducted by Huang et al. [12] have shown that the area specific resistances (ASR) of iron-based alloys coated with yttrium were 25% lower than for uncoated alloys, due to a smaller scale thickness and a stronger metal/scale interface.

Riffard et al. [13,14] characterized the oxide scale formed on yttrium-coated austentic stainless steel at 1000 °C using in situ X-ray diffraction (XRD) and scanning electron microscopy (SEM). In situ XRD experiments confirmed that the oxide scale, formed on the uncoated steel, was mainly composed of chromia and iron oxides, and predominantly grew by a diffusion process (parabolic law) after an initial transient stage of about 10 h. The yttrium effect on oxidation kinetic behaviour was characterized by the absence of an initial transient stage in the first hours and by a significant reduction in the scale growth rate. The presence of yttrium also suppressed the formation of iron oxide, which is an oxide that tends to crack and spall, further decreasing the conductivity and increasing the oxide growth rate. For steels coated through a dipping process into a sol–gel mixture, yttrium mixed oxides ($YCrO_3$ and $YCrO_4$) as well as chromia and spinel phases were identified in the oxide layer. In addition, silicon accumulation (~1 wt% Si is present in the steel), which is thought to promote a continuous layer of oxide formation, occurred at the steel/oxide interface. In contrast, steels coated using an ion implantation method did not form $YCrO_3$ and $YCrO_4$ in the oxide layer, and there was no accumulation of silicon at the steel/oxide interface.

Doping of the chromia phase in stainless steels to generate a semiconductor surface phase is another method for decreasing the oxide electrical resistance of interconnects. The doping effects of several metal oxides in chromia have been studied by different research groups under various experimental conditions (see summary in [12]). These substitutions have been shown to have a great impact on the conductivity of Cr_2O_3. The addition of NiO and MgO increased chromia conductivity, while the addition of ZnO, TiO_2 and WO_3 decreased conductivity. Huang et al. [12] tried to modify the conductivity of the Cr_2O_3 layer on Ebrite and AISI SAE 446 ferritic stainless steels by adding nickel oxides. Samples with nickel in the coatings consistently had lower area-specific resistance values, indicating that nickel decreased the electrical resistivity of the oxide.

Yttrium has been widely applied to various alloys including nickel-, cobalt- and iron-based alloys, but little has been done on its application in protecting lower Cr ferritic stainless steels (e.g., AISI-SAE 430 which contains 16–18 wt% Cr). A preliminary study [15] has shown that yttrium-containing coatings produced by sol–gel methods significantly reduced the growth rate of chromia in air at 750 °C. No electrical measurements were done on the oxides, however. In this work, yttrium, cobalt and mixed yttrium/cobalt coatings are applied to AISI-SAE 430 ferritic stainless steel. Cobalt is added as a potential p-type dopant for chromia. This work complements the studies performed with Ni coatings [12]. Uncoated and coated samples are annealed for up to 500 h and the oxidation behaviour is compared. The oxides are analyzed using XRD, scanning electron microscopy, thermogravimetry (TG) and area specific resistance measurements.

2. Experimental methods

2.1. Sample preparation

The substrate material selected for all coating experiments was AISI-SAE 430 stainless steel, hereafter referred to 430 SS, which has a thermal expansion coefficient similar to that for the SOFC electrolyte (YSZ). All specimens were cut from the same sheet of 430 SS except the specimens used for TG measurements, which were specially ordered because of the weight limitation of the TG instrument.

In order to prepare the coated samples, coupons, 2.5 cm × 2.5 cm in size, were laser cut from stainless steel pieces originally 10 cm × 10 cm × 0.1 cm. The coupons were then cleaned in 2% Citranox solution (Alconox) in an ultrasonic (Aquasonic 75HT) bath for 15 min, followed by rinsing in de-ionized water, soaking for one minute in pure ethanol and drying in air with a blow dryer. Following this cleaning procedure, the stainless steel coupons were dip coated in sol–gel solutions containing the appropriate precursor—$Y(NO_3)_3{\cdot}6H_2O$ (Alfa Aesar, 99.9% purity) and $CoCl_2{\cdot}6H_2O$ (Alfa Aesar, 99.9% purity). The solutions for the sol–gel coatings were 0.1 M in ethanol, and were prepared

based on the method used by Li [16]. The dipping process was carried out on a customized dip coater with a dipping speed of 10 cm min^{-1}. Samples were held in the solution for 1 min, and then withdrawn at a speed of 10 cm min^{-1}. The coated samples were initially dried at 180 °C for 15 min.

For each coating group (Y, Co, Y/Co), six coupons were prepared (i.e., 18 coupons in total). Ceramic blocks containing slots to hold the coupons in a vertical position were used to support the coupons while they were annealed. Annealing was done in air with a temperature ramp rate of 3 °C min^{-1}. A temperature of 750 °C was maintained for annealing times of 1, 10, 50, 100, 250 or 500 h.

2.2. Sample characterization

Each of the annealed coupons was cut into smaller pieces (~1 cm × 1 cm) with a diamond saw. These samples were analyzed with a variety of techniques. X-ray diffraction was performed using a Rigaku Multiflex X-ray Diffractometer, operated at 40 kV and 40 mA with a copper target. The samples were scanned over the range of $2\theta = 15$–$90°$, in steps of 0.020° and a scan speed of 0.5° min^{-1}.

Oxide microstructures (plan view and cross-section) were examined using a LEO 1450 Variable Pressure SEM, operating at 20 kV and equipped with an Oxford Instruments ultra thin window (UTW) X-ray detector. All SEM samples were coated with either gold or carbon in order to eliminate charging effects and to improve contrast. Both secondary electrons (SE) and backscattered electrons (BSE) were used for imaging to provide topographic (SE) and atomic number (BSE) contrast. Quantitative microanalysis was obtained through energy dispersive X-ray (EDX) spectroscopy, using a standardless approach.

Cross-section samples for SEM analysis were prepared using standard metallographic techniques. A piece, ~2 mm × 5 mm, was sectioned from an oxidized steel sample and glued to a piece of Si of the same size. The two pieces were then glued to additional Si pieces producing a "raft-like" structure. These rafts were polished with a series of increasingly finer grit SiC papers, and finally 1 μm diamond paste. Polished samples were coated with carbon.

Interconnect electrical behaviour is usually characterized in terms of an area specific resistance, which is the product of a materials's electrical resistivity and its thickness. Since stainless steels have much lower resistivities than their oxides, the ASR value of the oxidized steel is essentially the product of the oxide thickness and the measured resistivity. The ASR measurement system has been described previously [17]. Briefly, the system consists of a four-point probe system set up inside a tube furnace with a constant current supply (Agilent E3610) and data recorder (Fluke Hydra Series II), both connected with platinum leads to the sample. Ceramic rods, under compression, were used to apply pressure to the "sandwich" structure during measurement.

Thermogravimetric analysis (Setsys 16/18, SETARAM Scientific Industrial) was used to determine weight changes of the specimens in air. Because of the measurement range of the device, the material for the specimens was special ordered. The thickness of the sheets was about 0.025 mm. The stainless steel was cut into 1 cm × 1 cm squares using a photographic cutter. These samples were cleaned using Citranox solution as described in Section 2.1, and then two samples were loaded in an alumina crucible. The environment for the TGA measurement was air (flow rate = 40 ml min^{-1}) and the heating rate was 10 °C min^{-1} to the annealing temperature (700, 750 or 800 °C), with a dwell time for each experiment of 100 h.

3. Results

3.1. SEM analysis

Fig. 1 shows SEM SE images for the 430 SS sample oxidized for up to 500 h at 750 °C. Oxidation begins at surface defects, i.e., regions of local high energy and preferred diffusion paths. After 10 h, oxidation is primarily along scratches remaining on the steel sheet after fabrication (Fig. 1a). For longer oxidation times, the oxide clearly decorates the steel grain boundaries, showing an average ferrite grain size of close to 10 μm (Fig. 1b). After annealing for 250 h (Fig. 1c), the ferrite grain boundaries became less visible as the oxide has thickened and become continuous. Surface oxide particles, octahedral in shape and 1–2 μm in size, were present on samples annealed for 500 h (Fig. 1d). Evidence of spallation was found on the surface (Fig. 1d), indicating that the oxide did not adhere well to the substrate.

Plan view images of the oxides on the coated 430 SS samples after annealing for 250 and 500 h are shown in Fig. 2. Higher magnification SEM plan view and cross-section images for 500 h of oxidation are shown in Figs. 3 and 4, respectively. Similar uncoated samples are included for comparison. For the cross-section images (Fig. 4), the top half of each image shows epoxy and/or gaps between the epoxy and sample. For all samples, including the uncoated stainless steel, two oxides were present—an oxide adjacent to the steel substrate and an oxide at the gas phase interface (surface oxide) (Fig. 4). The oxide adjacent to the steel substrate was the first oxide to form, and was Cr-rich with smaller amounts of Mn and Fe. The surface oxide was Cr and Mn rich, with a Cr:Mn atomic ratio as determined by EDX analysis that was close to 2:1, and also contained minor amounts of Fe. Based on the EDX results and the oxide morphology, the surface oxide is likely a Cr–Mn spinel phase, while the oxide adjacent to the steel substrate is likely Cr_2O_3 (chromia). This preliminary phase assignment is confirmed by XRD in Section 3.2.

The major differences among the various samples were in terms of oxide morphology and thickness. In particular, the surface oxide layer (spinel) is discontinuous for all samples except for the Co-coated steels (Fig. 4). In this case, a fairly continuous spinel layer has formed, with a thickness comparable to that for the chromia layer. Chromia layer thicknesses,

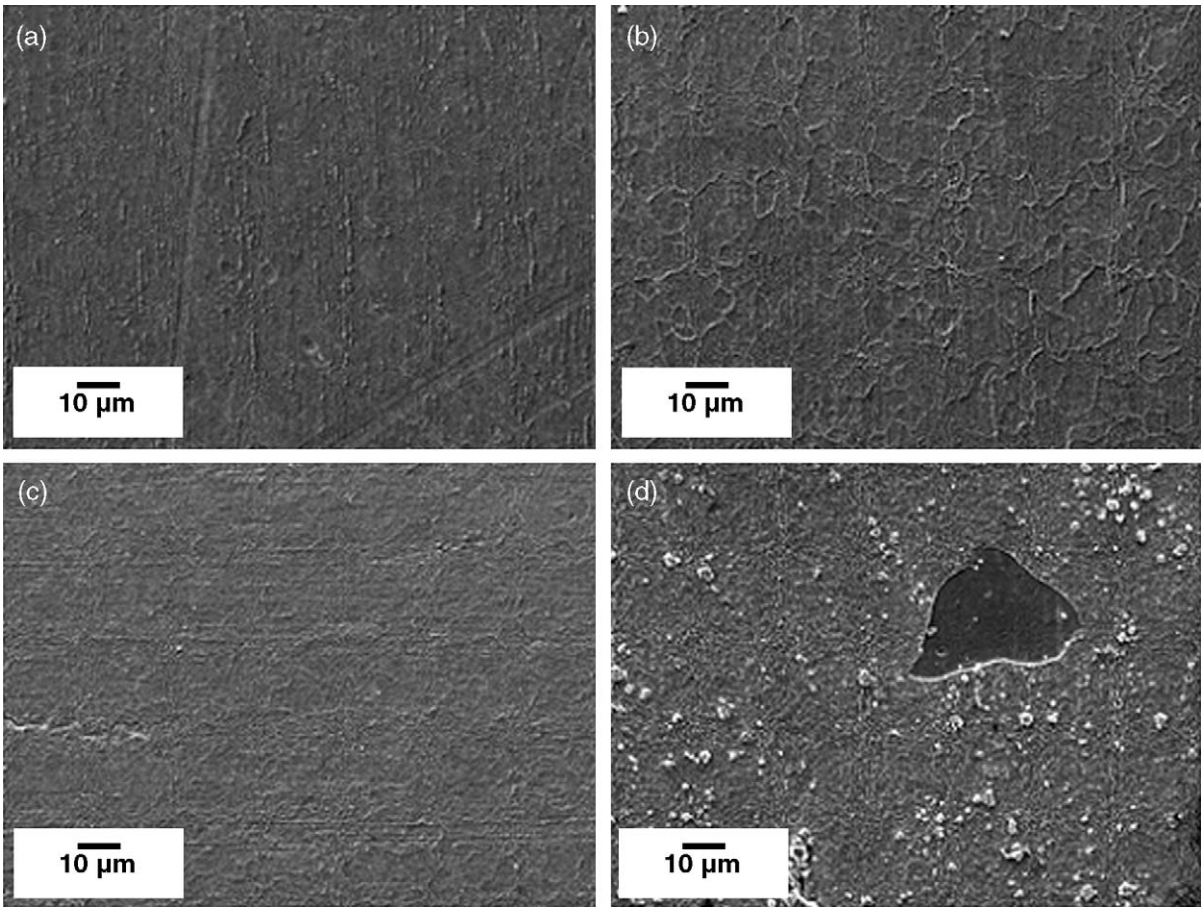

Fig. 1. SEM SE plan view images of uncoated 430 SS oxidized at 750 °C: (a) 10 h; (b) 100 h; (c) 250 h; (d) 500 h.

for all samples, for 250 and 500 h oxidation times are shown in Table 1. The errors in these values are less than ±6%. The Co-coated samples had the largest deviations in thickness. The uncoated and Co-coated samples (Fig. 4a and c) had the thickest chromia layers, while the Y-coated sample had the thinnest chromia layer (Fig. 4b) with the Y/Co coating showing the next thinnest chromia layer (Fig. 4d).

For the Y-coated samples (Fig. 2a and b), the spinel particles were 1–3 μm in size, while the chromia layer had a grain size less than 0.5 μm (Fig. 3b). The number of spinel particles increased with annealing time from 250 to 500 h. Yttrium was located only in the chromia layer and not in the surface spinel particles.

As mentioned above, the morphology of the Co-coated samples was quite different than that of either the uncoated samples or the Y-coated samples (Fig. 2c and d). Significant oxidation, even more than that present on the uncoated samples, was apparent after only 1 h of annealing. After 250 and 500 h of annealing, oxide growth was prevalent along ferrite grain boundaries (Fig. 2c and d) with two different oxide particle morphologies (Fig. 3c). The smaller particles (0.2–0.5 μm in size) were octahedral in shape and mainly grew along the ferrite grain boundaries. These primarily contained Cr and O, with smaller amounts of Mn, and were likely chromia. The larger particles (2–3 μm in size) were more irregularly shaped and formed away from the grain boundaries. These had a Cr:Mn ratio close to 2:1, which is indicative of Cr–Mn spinel. Cobalt was mainly detected in the spinel phase, although low levels were likely present in the chromia as well. The presence of Co, at low concentrations, was difficult to confirm by EDX, because its K_α X-ray peak overlaps with the K_β peak for Fe.

For the combined Y/Co binary coatings, the oxide morphology (Fig. 2e and f) was similar to that for the Y-coated samples. The major difference was a thicker chromia layer (Fig. 4 and Table 1). After annealing for 1–10 h, some of the coating elements had segregated to the ferrite grain boundary areas. Low levels of yttrium were frequently detected in the chromia layer by EDX analysis.

Table 1
Summary of adjacent oxide (chromia) thicknesses on specimens with different coatings

Specimen	250 h treatment (μm)	500 h treatment (μm)
430 SS	1.15	1.55
Y	0.30	0.40
Co	1.15	2.25
Y/Co	0.55	0.75

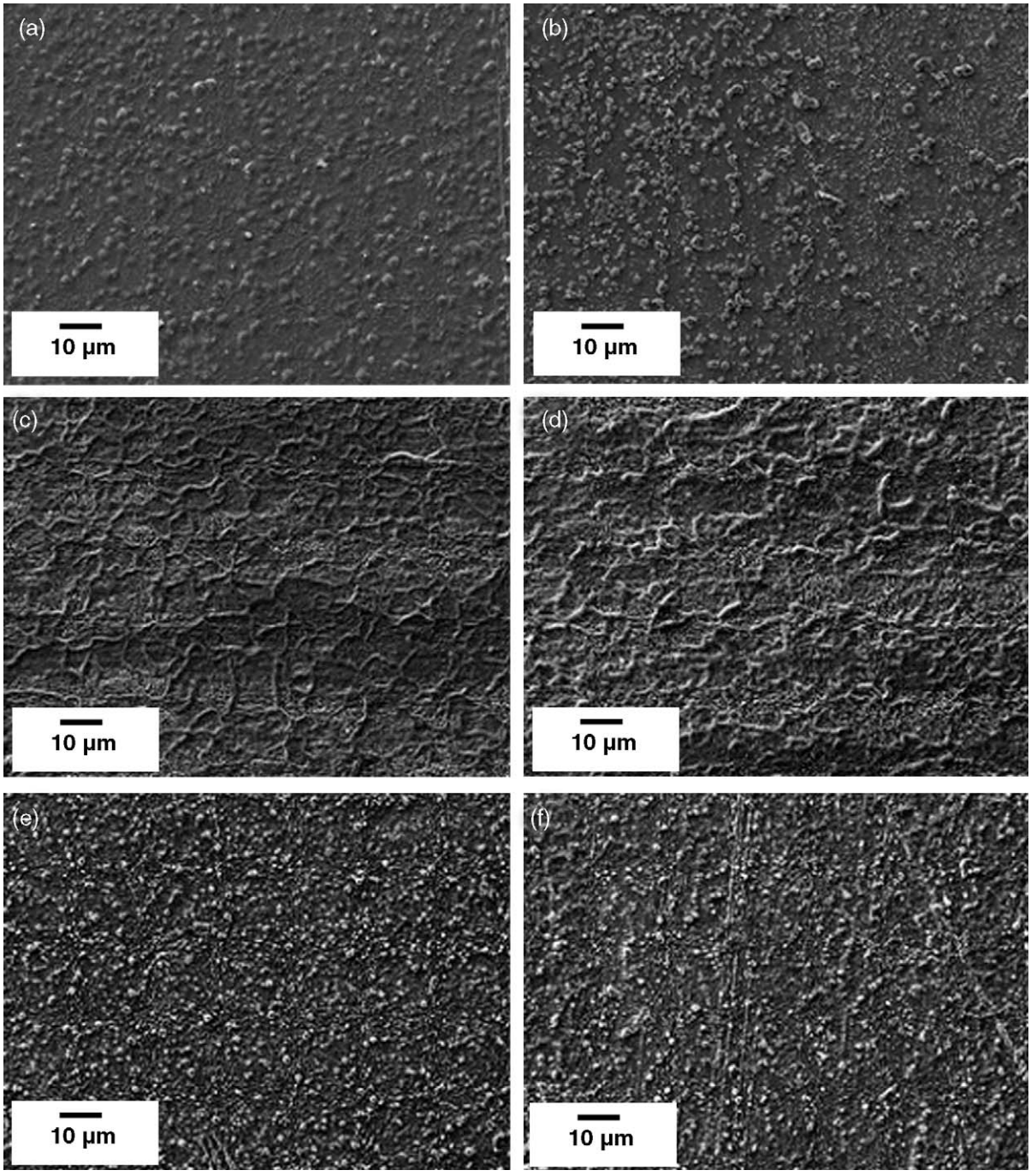

Fig. 2. SEM SE plan view images of coated 430 SS oxidized at 750 °C for 250 and 500 h, respectively: (a and b) Y-coated; (c and d) Co-coated; (e and f) Y/Co-coated.

3.2. Oxide phase identification by XRD

All phase identification was done by indexing XRD patterns to files in the JCPDS database [18]. XRD spectra for the uncoated 430 SS annealed for times between 1 and 500 h are shown in Fig. 5. The peaks match with Cr–Mn spinel (approximate composition corresponds to $MnCr_2O_4$) and chromia, which is consistent with the EDX data. EDX analysis also showed that Fe was present in the chromia phase. The Cr_2O_3–Fe_2O_3 phase diagram indicates that Cr_2O_3 and Fe_2O_3 are mutually soluble for the temperatures of interest in this work [19]. Both phases have the same crystal structure (hexagonal) and similar lattice parameters; $a = 0.4959$ nm and $c = 0.1.3594$ nm for Cr_2O_3 and $a = 0.5036$ nm and $c = 1.3749$ nm for Fe_2O_3 [18]. Therefore, the chromia phase could be written as $(Cr,Fe)_2O_3$. In the initial stages of oxidation only $(Cr,Fe)_2O_3$ peaks (peaks labelled 2 in Fig. 5), other than ferrite substrate peaks (labelled as 1 in

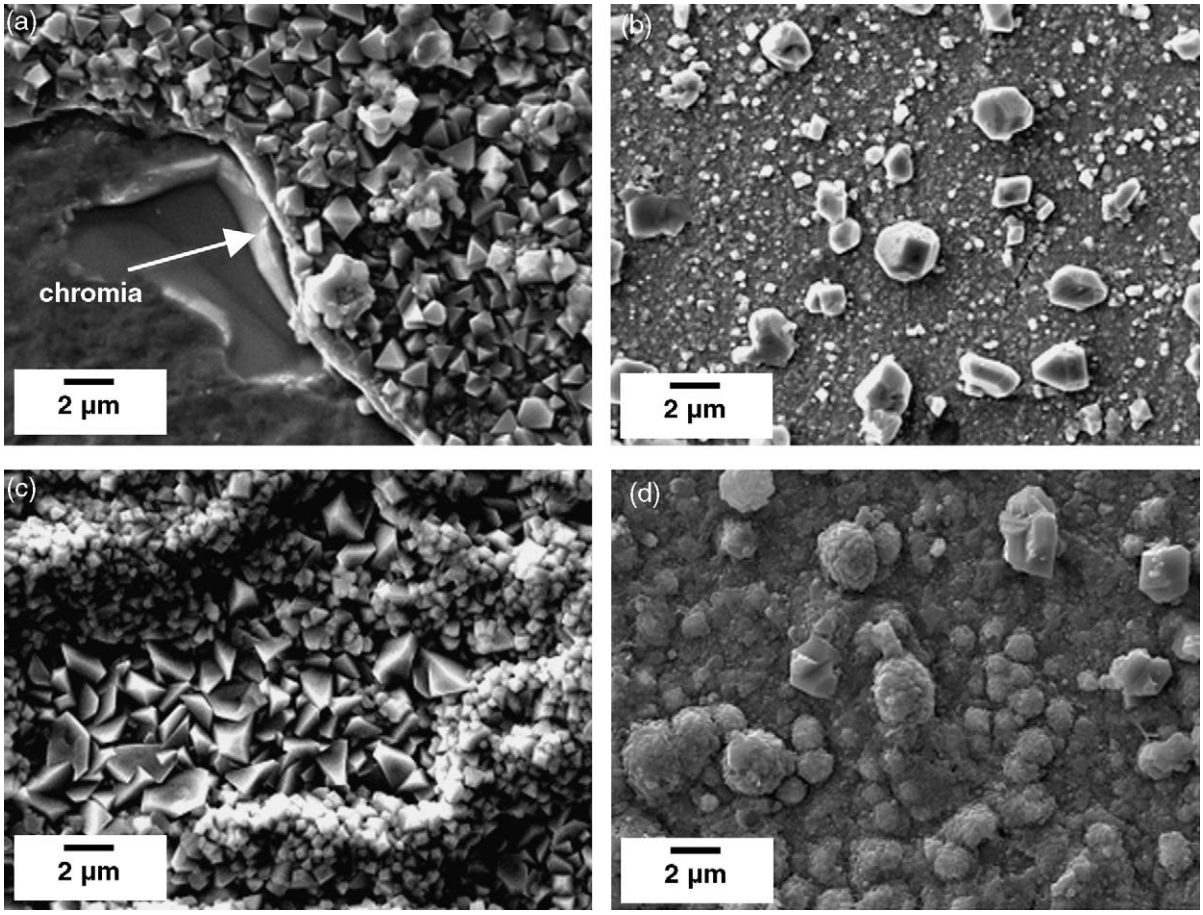

Fig. 3. Higher magnification SEM plan views images of samples oxidized for 500 h at 750 °C: (a) 430 SS; (b) Y-coated 430 SS; (c) Co-coated 430 SS; (d) Y/Co-coated 430 SS.

Fig. 5), are evident in the XRD spectra. After 50 h of annealing, spinel peaks are evident (peaks labelled 3 in Fig. 5). These results are clear evidence that chromia forms first, followed by spinel at longer oxidation times, and that spinel is the surface oxide.

The XRD spectra for Y- and Y/Co-coated samples after annealing times between 1 and 500 h are shown in Figs. 6 and 7, respectively. The main oxide phases again were chromia and Cr–Mn spinel. Comparison with the uncoated 430 SS XRD patterns shows that there are additional peaks in the spectra for the Y-containing samples. There were small peaks at $2\theta = 25^\circ$ and at $2\theta = 58^\circ$, which may be from $YCrO_4$. Other peaks for $YCrO_4$ overlap with chromia peaks, so definitive identification was not possible. $YCrO_4$ is one of the yttrium chromium compounds commonly found in Y-containing coatings [14,20]. Its formation may hinder ion diffusion and further decrease the oxidation rate. There were no individual CoO and Y_2O_3 phases detected. All XRD patterns for the Y- and Y/Co-coated samples (even after 500 h of annealing) had strong reflections from the base material (430 SS), which is an indication that the oxides were not as thick as those for 430 SS and the Co-coated samples. As with the uncoated 430 SS samples, the chromia peaks were predominant initially, with the spinel peaks becoming stronger at longer annealing times.

The XRD spectra for the Co-coated samples are shown in Fig. 8. Both chromia and Cr–Mn spinel were detected, as was the case for the other coated and uncoated samples. The main difference was in the diffraction intensities of the phases. After annealing for 500 h, the diffracted intensity from the base material (ferrite) almost disappeared, while spinel peak intensities significantly increased. This result is an indication that the spinel phase was quite thick (confirmed by SEM imaging). Another noticeable difference was apparent over the range of annealing times (Fig. 8). The initial oxide peaks matched better with Fe_2O_3 than Cr_2O_3 for shorter annealing times (<10 h) and shifted towards Cr_2O_3 as annealing times increased. This is shown in Fig. 9, in particular for the 104 (at $2\theta \sim 33$–33.5°) and 113 (at $2\theta \sim 41$–41.5°) peaks for $(Cr,Fe)_2O_3$. No CoO single phases were detected.

3.3. Thermogravimetric results

Oxide kinetic studies were done on three of the samples, i.e., uncoated 430 SS, Y- and Y/Co-coated stainless steels. The Co-coated steels were not investigated, since they suf-

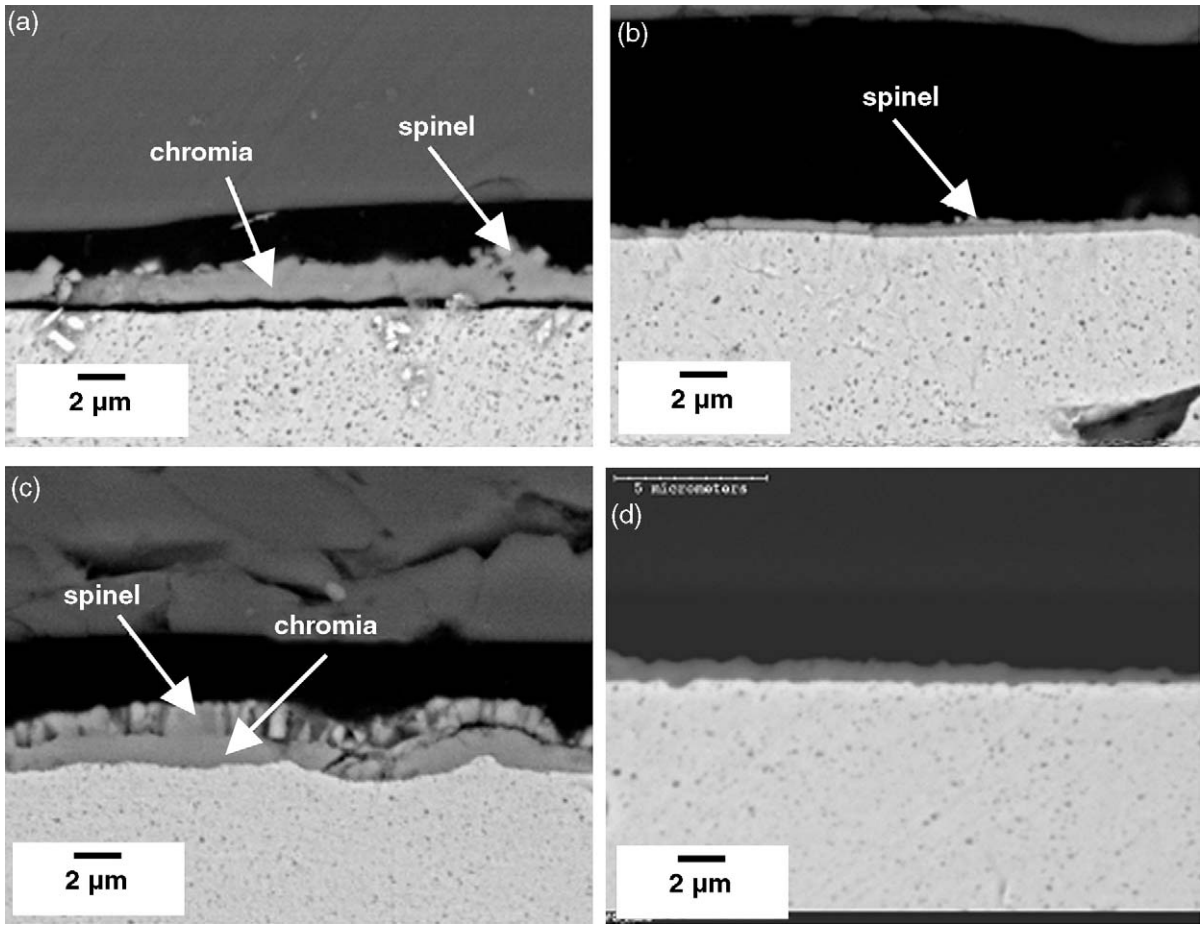

Fig. 4. SEM BSE cross-section images of samples oxidized for 500 h at 750 °C: (a) 430 SS; (b) Y-coated 430 SS; (c) Co-coated 430 SS; (d) Y/Co-coated 430 SS.

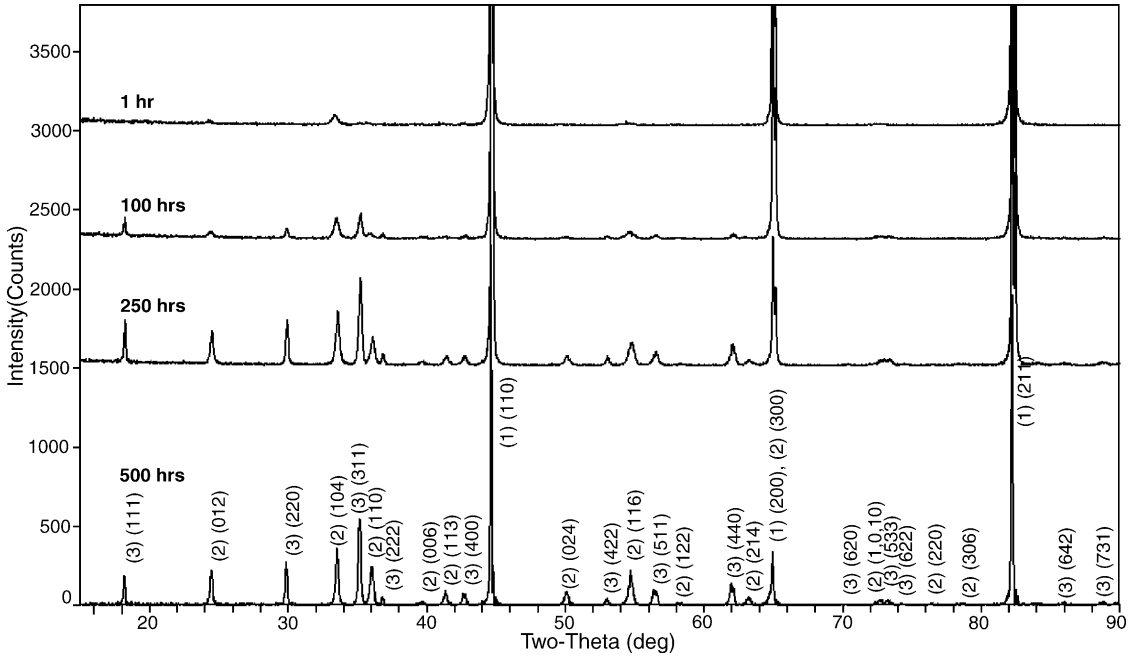

Fig. 5. XRD patterns for uncoated 430 SS oxidized for 1, 50, 250 and 500 h at 750 °C: (1) ferrite; (2) $(Cr,Fe)_2O_3$; (3) $(Mn,Cr)_3O_4$.

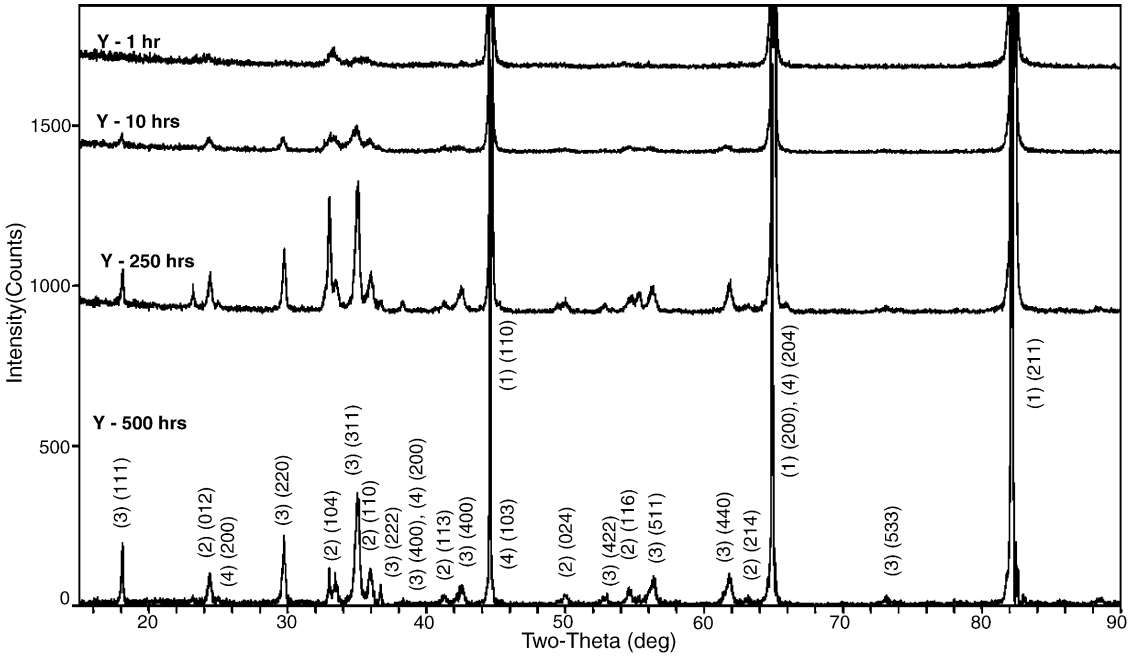

Fig. 6. XRD patterns for Y-coated 430 SS oxidized for 1, 10, 250 and 500 h at 750 °C: (1) ferrite; (2) $(Cr,Fe)_2O_3$; (3) $(Mn,Cr)_3O_4$; (4) $YCrO_4$.

fered from the most oxidation and had high ASR values. As such, Co alone was not deemed to be a potential coating candidate. The change in mass with annealing time at different temperatures for the uncoated, Y- and Y/Co-coated samples is given in Fig. 10. As expected, the samples gained more mass (more oxide formation) at higher annealing temperatures. The TG data was fit to a Tammann-type parabolic equation, $X = K_p t + X_0^2$, where X denotes the total scale thickness, t the oxidation/annealing time, X_o the initial scale thickness (X_o is set equal to zero here) and k_p is the parabolic rate constant. The data for annealing temperatures of 700 and 750 °C show parabolic behaviour, while the mass gain at 800 °C deviates from a parabolic behaviour at longer oxidation times (>30–40 h). The deviation is most significant for the Y/Co-coated steel.

The rate constants (k_p) obtained from the plots in Fig. 10 can be fit to an Arrhenius expression to determine the activation energies for the oxide formation process on each of

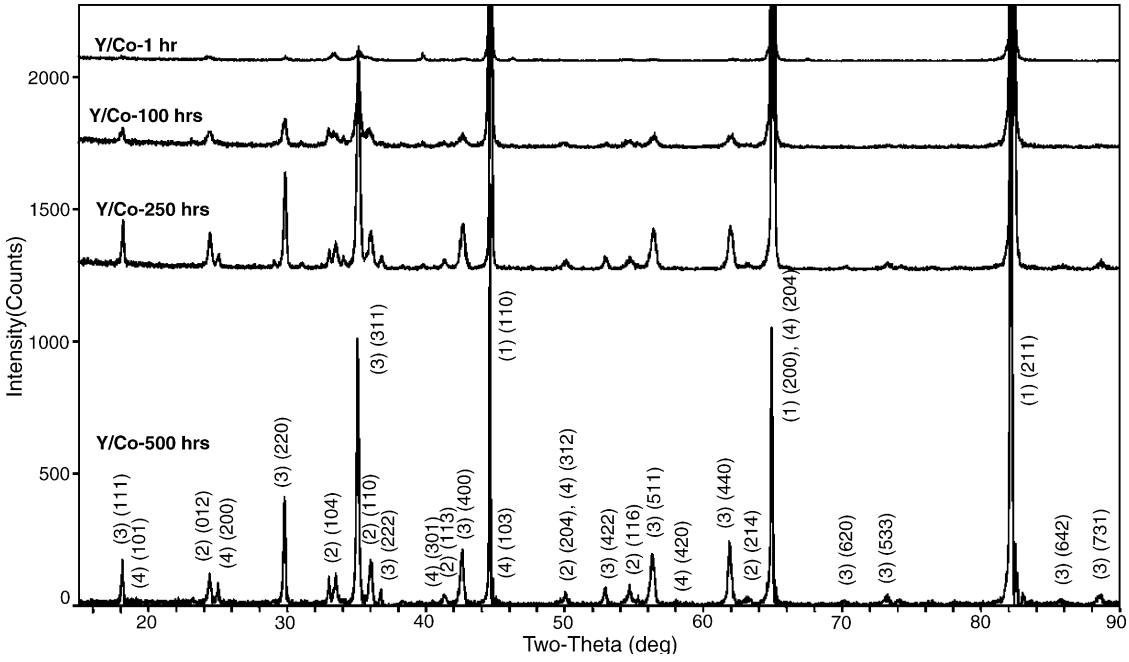

Fig. 7. XRD patterns for Y/Co-coated 430 SS oxidized for 1, 100, 250 and 500 h at 750 °C: (1) ferrite; (2) $(Cr,Fe)_2O_3$; (3) $(Mn,Cr)_3O_4$; (4) $YCrO_4$.

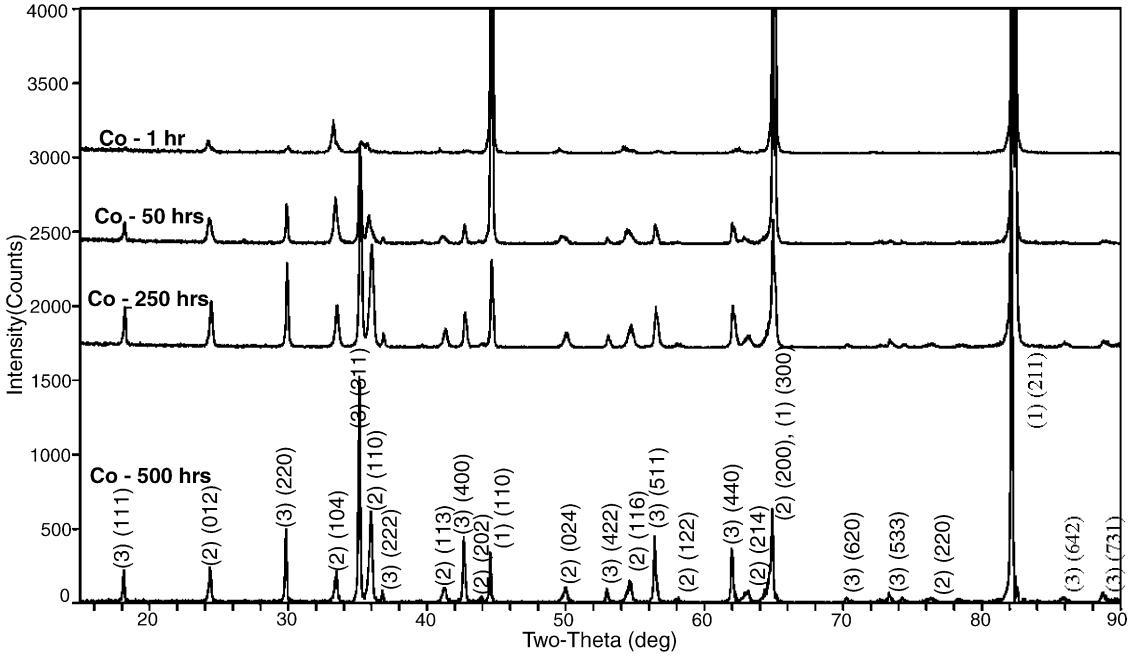

Fig. 8. XRD patterns for Co-coated 430 SS oxidized for 1, 50, 250 and 500 h at 750 °C: (1) ferrite; (2) $(Cr,Fe)_2O_3$; (3) $(Mn,Cr)_3O_4$.

the samples (Fig. 11). For oxidation at 800 °C, only the data from the first 30 h was used to determine the rate constant. The selection of 30 h was somewhat arbitrary and had little effect on the activation energy for the uncoated steel. A value of 250–255 kJ mol^{-1} was determined (using 30 or 40 h) and compares favourably with that for the formation of Cr_2O_3 on Cr, i.e., 255 kJ mol^{-1} [25]. For the coated steels, the $\ln k_p$ versus $1/T$ plots showed significant scatter, particularly for the Y-coated samples; nevertheless, activation energies were calculated as 160 and 230 kJ mol^{-1} for Y- and Y/Co-coated samples, respectively. Activation energies were 175 and 215 kJ mol^{-1} for Y- and Y/Co-coated samples, respectively, if 40 h was used as the oxidation time for 800 °C. The activation energies for the Y- and Y/Co-coated samples are lower than the value for the uncoated steel, which would imply that oxide formation is easier. This is an interesting result considering the fact that the oxides on the Y- and Y/Co-coated samples are thinner than the oxides on uncoated 430 SS. Pre-exponential factors (i.e., the frequency factors, k_o) were also calculated and these are 3.4×10^8,

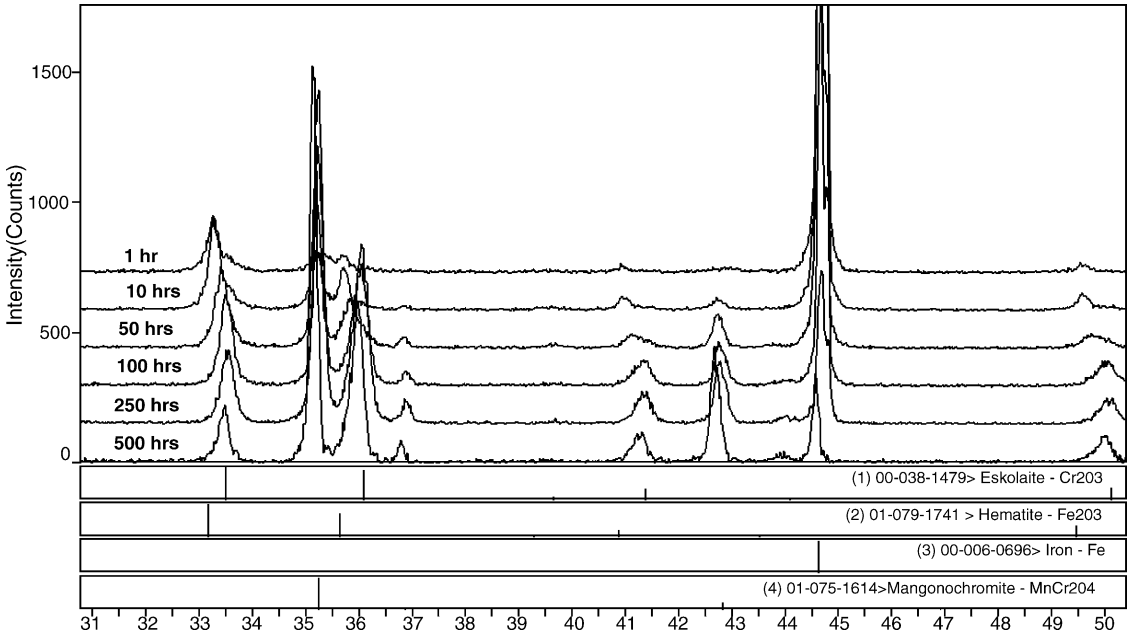

Fig. 9. XRD patterns for Co-coated 430 SS oxidized for 1, 10, 25, 50, 100, 250 and 500 h at 750 °C.

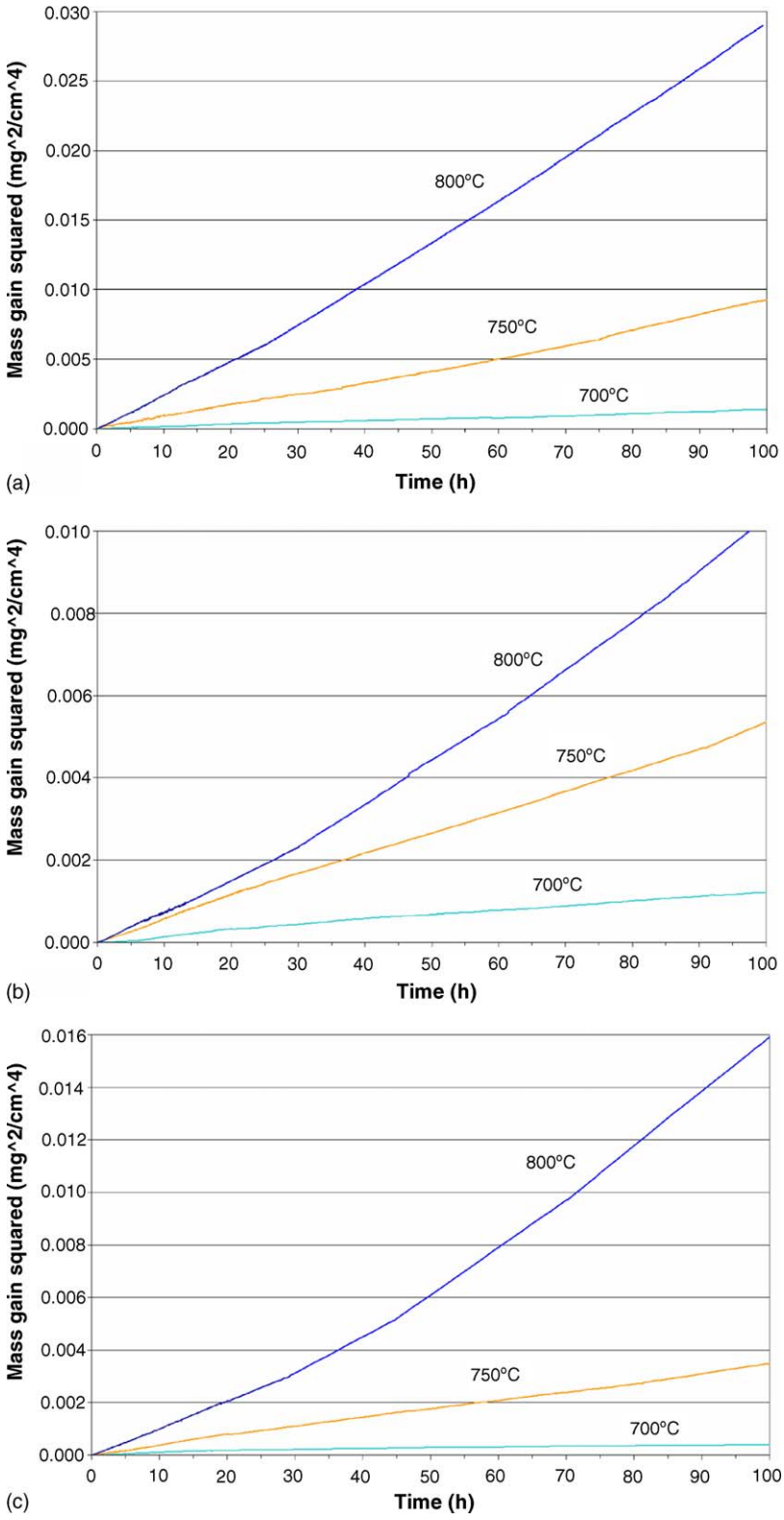

Fig. 10. TG (mass gain) data as a function of time for (a) uncoated; (b) Y-coated; (c) Y/Co-coated 430 SS.

4.5×10^3 and 2.1×10^7 mg^2 (cm^4 h)$^{-1}$ for the uncoated, Y- and Y/Co-coated steels, respectively. Another interesting feature is apparent if the mass gain data is plotted as a function of temperature, for oxidation times of 100 h (Fig. 12). The uncoated steel has the largest mass gain at all temperatures, while the Y/Co-coated steels have the lowest mass gains at 700 and 750 °C and the Y-coated steels have the lowest mass gain at 800 °C.

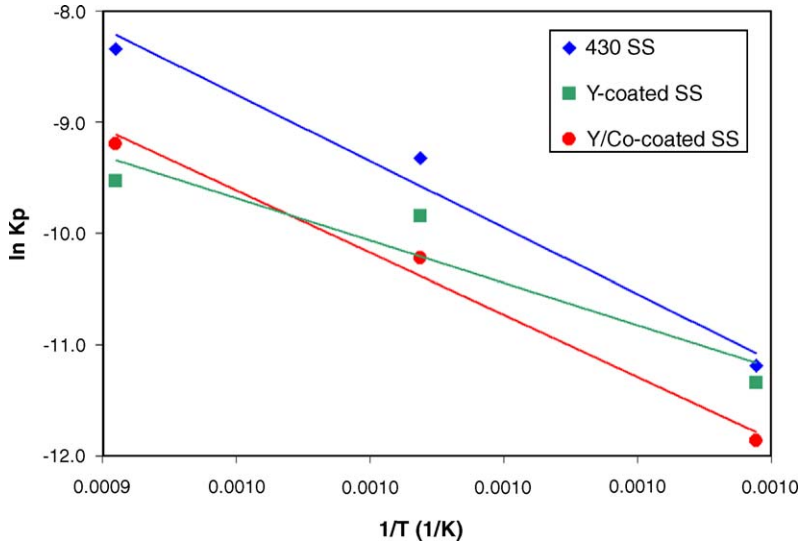

Fig. 11. Plots of $\ln(k_p)$ vs. $1/T$ for uncoated 430 SS, Y-coated 430 SS and Y/Co-coated 430 SS.

3.4. ASR measurements

The major challenge in obtaining reliable area specific resistivity measurements was ensuring good contact during assembly and testing. A wide temperature range, 650–850 °C, was used to test most samples in order to check data reliability. Resistivities varied by less than ±5% for a given temperature if ASR values were higher than 30 mΩ cm^2 and approximately ±15% for ASR values lower than 30 mΩ cm^2 (i.e., Y coatings). Spallation was found in the uncoated 430 SS samples annealed for 250 and 500 h, and also in the Co-coated samples annealed for 500 h. It was not possible to get accurate ASR data from spalled samples and, thus, ASR results for these samples are not reported. ASR values at 750 °C, a typical operating temperature for an SOFC, as a function of annealing time are plotted in Fig. 13, with values determined at 750 °C shown in Table 2.

Table 2
ASR results for various coatings at 750 °C (mΩ cm^2)

750 °C	430	Y	Co	Y/Co
500 h	Spalled	21	Spalled	23
250 h	Spalled	18	71	16
100 h	69	14	49	10

The 430 SS and Co-coated samples had the highest ASR values as was expected according to the SEM thickness measurements presented in the previous section. The ASR values for the Y- and Y/Co-coated samples were over four times

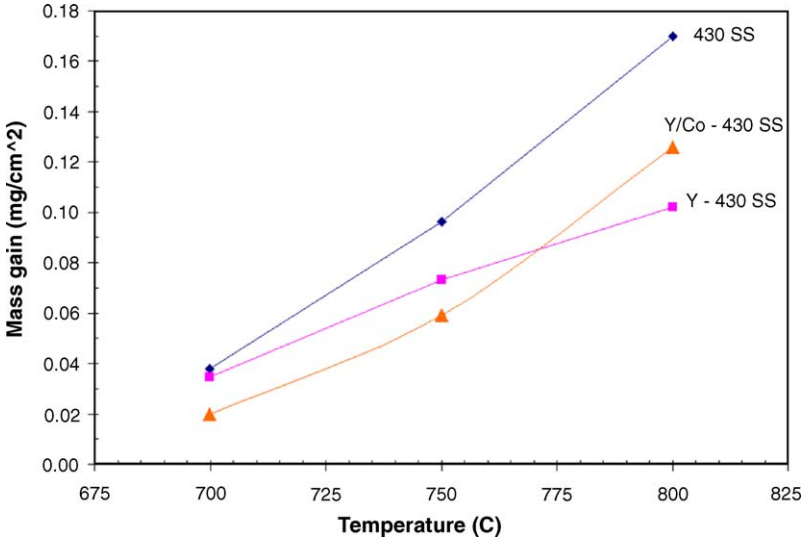

Fig. 12. Plots of mass gain vs. temperature for uncoated 430 SS, Y-coated 430 SS and Y/Co-coated 430 SS. The oxidation time in all cases was 100 h.

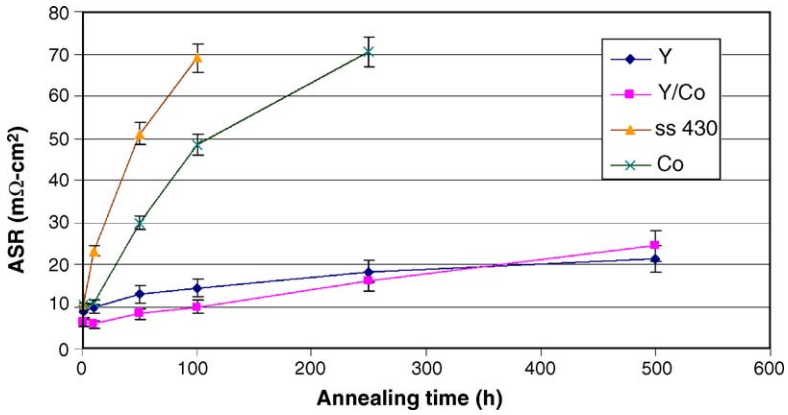

Fig. 13. ASR results for uncoated 430 SS, Y-coated 430 SS, Co-coated 430 SS and Y/Co-coated 430 SS, measured at 750 °C.

Table 3
Apparent resistivities for coatings after annealing for 250 h

750 °C	430	Y	Co	Y/Co
ASR for 250 h specimens (mΩ cm^2)	N/A	18	71	16
Overall oxide thickness (μm)	0.80	0.30	1.15	0.55
Apparent resistivity (Ω m)	N/A	3	3	1.5

smaller than those for the other samples. In fact, ASR values for Y- and Y/Co-coated samples, after 500 h of annealing, were more than three times lower than the values for uncoated 430 SS after 100 h of oxidation. Apparent resistivities were estimated by dividing the ASR values by two times the thickness of the oxide layer (as given in Table 3) to account for oxide formation on both sides of the samples. Both the spinel and chromia oxide thicknesses were used for the Co-coated samples, while only the chromia layer thickness was used for the Y- and Y/Co-coated samples since the spinel was discontinuous. The calculated apparent resistivities after an annealing time of 250 h are 3, 3 and 1.5 Ω m for Y-, Co- and Y/Co-coated samples, respectively.

4. Discussion

4.1. Uncoated 430 SS

Normally, metal oxidation begins by oxygen chemisorbing on the metal surface until a complete two-dimensional oxide layer covers the metal. After the monolayer forms, discrete nuclei of three-dimensional oxides begin appearing at structural defects, such as grain boundaries, impurities and dislocations [22].

The oxidation of uncoated 430 SS in this study followed the typical oxidation process outlined in the previous paragraph and is shown schematically in Fig. 14. To simplify the schematics, only Cr and Mn oxidation are shown in the figure, although Fe is present in both the chromia and the spinel phases. Ferrite grain boundaries are evident in Fig. 1b after 100 h oxidation. Chromium diffusion occurs primarily along the ferrite grain boundaries along with some bulk diffusion, so that initially more Cr_2O_3 forms at the intersection of the ferrite grain boundaries with the surface. Once a continuous

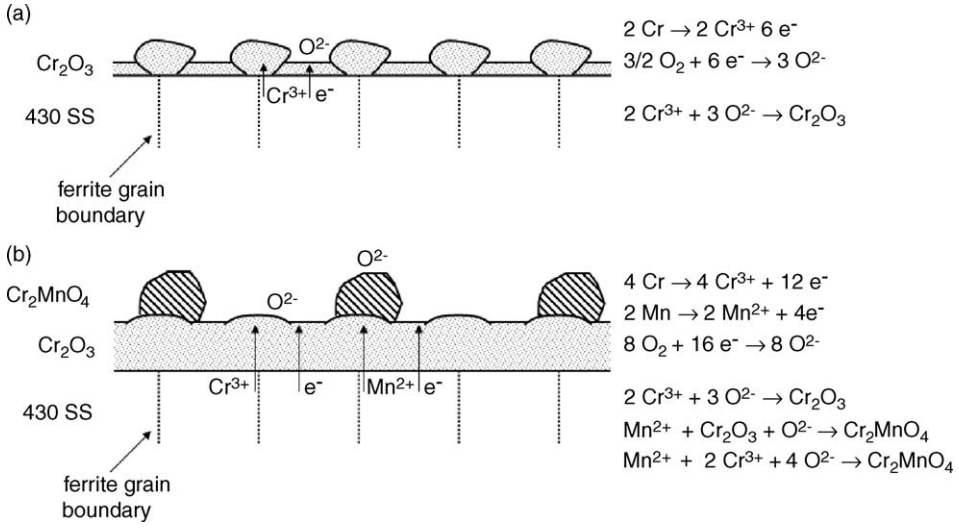

Fig. 14. Schematic of 430 SS oxidation process. (a) <50 h and (b) >50 h.

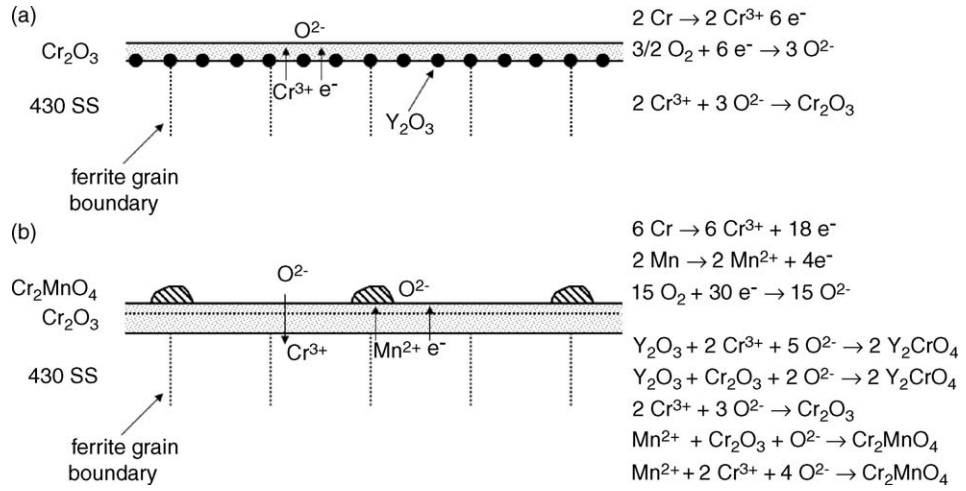

Fig. 15. Schematic of Y-coated 430 SS oxidation process. (a) ∼10 h and (b) >50 h. The dashed line in (b) represents the original position of the Y_2O_3 particles.

layer of chromia forms, further oxide growth requires the oxidation of Cr to Cr^{3+} ions plus electrons, both of which move through the oxide layer to the oxide/air interface. Then the Cr^{3+} ions react with reduced O_2 (O^{2-} ions) to form Cr_2O_3 (Fig. 14a). At the same time, Mn and Fe ions (Mn^{2+} and Fe^{3+}) diffuse through the chromia layer and react at the surface to form the spinel phase (Fig. 14b). Based on the EDX results, the ratio of Cr:Mn in the spinel phase is assumed to be 2:1. The chromia layer increases in thickness with increasing annealing time and eventually spalls from the surface. The spinel phase remains discontinuous. Although O^{2-} ions can diffuse through the chromia layer and react with Cr^{3+} ions to form additional chromia at the chromia/steel interface, the major diffusing species is Cr^{3+} so that chromia formation at the chromia/air interface dominates.

The reason that Mn-containing spinel forms on the surface of chromia may be related to the diffusion rates of transition elements through chromia. According to a study of different elements diffusing in chromia layers grown on Fe–20Cr and Fe–20Cr–12Ni model alloys by Lobnig et al. [23], Mn^{2+} is the fastest diffusing element in chromia. The diffusion coefficient values for Cr, Fe and Ni ions are similar, but lower than that for Mn, which could explain why the Mn-rich spinel becomes one of the main oxide phases, even though the steels contain less than 1% Mn.

4.2. Y-coated 430 SS

Y-coated samples demonstrated different oxidation behaviour. For samples annealed for 250 and 500 h, Y was detected in the chromia underlayer/adjacent oxide (both at and away from the grain boundaries), which implies that Y had dissolved in the chromia. Cross-section images show a notably thinner chromia layer for the Y-coated samples compared with the uncoated 430 SS, as well as less spinel phase (Fig. 4a and b). The formation of $YCrO_4$, detected by XRD (Fig. 6), may contribute to the oxidation resistance. Overall, metal oxidation was suppressed by applying the yttrium coating.

The oxidation process is shown schematically in Fig. 15. Nucleation theory has previously been proposed to explain the reactive element (RE, e.g., Y) effect during the early stages of oxidation [24]. Reactive element oxide particles present on the metal surface are proposed to act as nucleation sites for the first-formed oxides, thus, greatly increasing the number of nuclei compared with the uncoated steel. Without the RE coating, nucleation sites are only at the grain boundaries, impurities and dislocations. The well-dispersed Y coating decreases the inter-nuclei spacing dramatically (Fig. 15a) and increases the number of oxide nuclei. The net result is a finer chromia grain size (Fig. 3b) and the time required for the nuclei to grow laterally to form a continuous oxide layer is reduced. After the formation of a dense surface layer, oxide growth is then controlled by cation (Cr^{3+}) diffusion through the chromia grain boundaries, since grain boundaries are the favoured paths for diffusion. The Y appears to play a role in reducing the oxidation rate. The exact mechanism is unclear at this time; however, Y_2O_3 or Y–Cr oxides may block grain boundary diffusion paths. In this work, no Y_2O_3 was detected, but $YCrO_4$ was detected by XRD. The reduction in the Cr^{3+} diffusion rate results in O^{2-} becoming the main diffusing species through the chromia, so that subsequent chromia formation occurs at the chromia/steel interface (Fig. 15b). The inward diffusion of oxygen anions facilitates the formation of a more compact and adherent oxide layer. Since cation diffusion is suppressed (including Mn^{2+} and Fe^{3+}), less spinel forms compared with the uncoated 430 SS (Fig. 3).

The presence of Y has a significant effect on ASR. ASR can be decreased by reducing the resistivity of the oxide and/or decreasing the oxide thickness. The primary effect here is oxide thickness reduction, although there is a slight decrease in oxide resistivity. For the same annealing duration condition, Y-coated 430 SS has about 25% the oxide thickness compared with uncoated 430 SS (Table 1) and an ASR

value less than 25% of the ASR value of the uncoated 430 SS (Table 2).

4.3. Co-coated 430 SS

Co-coated stainless steels exhibited a faster oxide growth rate compared with the other coated and uncoated stainless steel. As with the other samples, two oxide layers formed (Fig. 4c), i.e., chromia and spinel. A major difference was that the spinel layer was essentially continuous and considerably thicker than that formed in the other samples. XRD results also showed more intense spinel peaks relative to chromia and relative to the other samples (Fig. 8).

The reason for the increase in spinel formation, due to the presence of Co, is not clear at this time. However, Co appears to affect the Fe levels in chromia during the initial oxidation stages. XRD results (Fig. 9) show that the initial oxide to form (<10 h) is closer to Fe_2O_3 in composition and becomes more Cr-rich as oxidation proceeds. Chromia studies by Oswald and Grabke [25] indicated that to provide protection, Cr_2O_3 must grow relatively rapidly to a dense, sufficiently thick scale. Fe_2O_3 is much less dense than Cr_2O_3 and could facilitate cation diffusion (Cr^{3+}, Mn^{2+} and Fe^{3+}) to the surface allowing more spinel to form (Fig. 16).

The total oxide thickness for the Co-coated samples was almost twice that of the uncoated 430 SS. However, the ASR was not proportionally higher. The higher conductivity for the Co-containing coatings may be due to Co doping (Co^{2+}) of chromia, although most of the Co is believed to be in the spinel phase according to the EDX results. The amount of Co dissolved in chromia may be below the detectability limit of the EDX technique but still sufficient to have an effect.

Another contribution to the lower resistivity of Co-coated stainless steels is that Co may lower the resisitivity of the spinel phase. Comparison of the oxide thicknesses, for uncoated 430 SS and Co-coated 430 SS in Fig. 4 and Table 1, shows that the chromia thickness is almost the same (e.g., oxidation times of <250 h) while the spinel thickness is much greater for the Co-coated steel. $CoCr_2O_4$ is known to have an approximately order of magnitude lower resistivity than $MnCr_2O_4$ (0.52 Ω cm versus 3.2–7.9 Ω cm at 750 °C) [26].

4.4. Y/Co-coated 430 SS

The oxidation process for these samples was very similar to that for the Y-coated stainless steels (Fig. 15). The major difference was in the amount of chromia and spinel formed. For higher oxidation temperatures and longer oxidation times, Y-coated steels were more resistant to oxidation than Y/Co-coated steels (Figs. 4 and 15). EDX analysis showed that Y was mainly dissolved in the chromia and Co was mainly found in the large spinel particles. No individual CoO and Y_2O_3 phases were identified (Fig. 7).

The properties of the Y/Co-coated steels may be affected by both elements. The chromia thickness after oxidation for 250 h at 750 °C (Fig. 4d and Table 1) was the second lowest (Y-coated steels displayed the best overall oxidation resistance), i.e., about half that for uncoated 430 SS. The apparent resistivity at 750 °C for the Y/Co-coated sample was 1.5 Ω m, which is approximately half the value for the Y-coated sample (3 Ω m). This is additional evidence that Co lowers the resistance of chromia through doping.

4.5. Oxidation kinetics

Two oxides formed during the oxidation process for all samples examined: a continuous chromia layer and a discontinuous spinel phase. The exception is the Co-coated samples, where the spinel layer was quite continuous. Chromia was the dominant layer (at 700 and 750 °C) for all but the Co-coated samples, although part of the weight gain was caused by spinel formation. At 800 °C, the kinetic curves

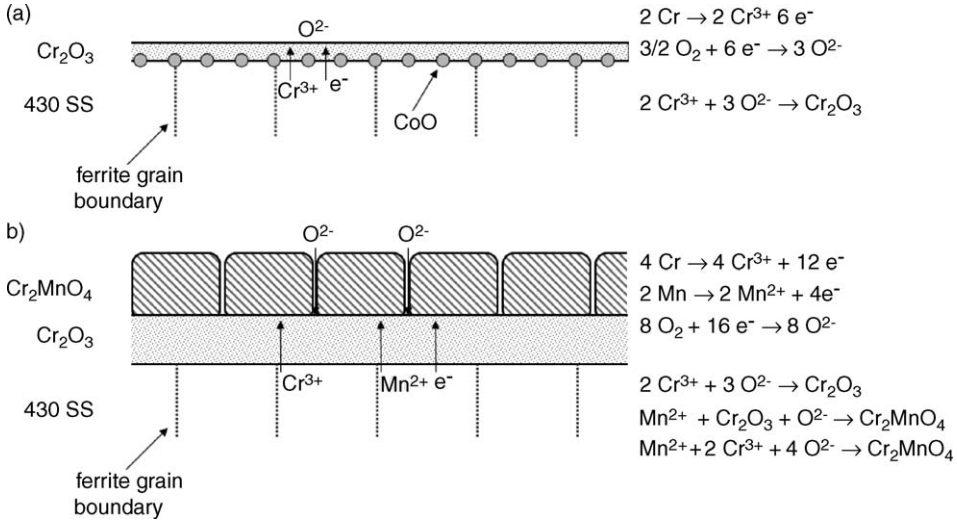

Fig. 16. Schematic of Co-coated 430 SS oxidation process. (a) <10 h and (b) >50 h.

for the uncoated, Y- and Y/Co-coated samples deviated from parabolic behaviour, exhibiting paralinear behaviour. The deviation was most pronounced for Y/Co-coated stainless steel. The switch to paralinear kinetics is likely due to increased formation of the unprotective spinel phase.

The activation energy determined in this work for oxidation of uncoated 430 SS (250 kJ mol^{-1}) is the same as that for cation (Cr^{3+}) diffusion in pure Cr_2O_3 (255 kJ mol^{-1}) [21]. The activation energies for Y- and Y/Co-coated 430 SS (160–175 and 215–230 kJ mol^{-1}, respectively) are lower than that for the uncoated steel. This difference is significant for the Y-coated steel and may be an indication that the oxidation mechanism is different for the coated steels. The lower activation energy, relative to the uncoated steel, did not result in a higher oxidation rate for the Y-containing coatings, as might be expected. Instead, the presence of Y significantly reduced the pre-exponential factor in the Arrhenius equation, effectively lowering the rate constant. The cause of this change is not clear at this time. For the Y/Co-coated steels, the presence of Co may have offset somewhat the effect of Y.

The activation energy trend is consistent with the study of Y and Ni coatings on other ferritic stainless steels, i.e., 446 SS and Ebrite, by Huang et al. [12]. Their study indicated that application of Y and Y/Ni coatings could decrease the weight gain rate at 800 °C and decrease the activation energy for oxide formation. Activation energies for uncoated, Y/Ni- and Y-coated steels were 87, 85 and 68 kJ mol^{-1}, respectively. These values are significantly lower than the values obtained in this study. This difference may be due, in part, to different measurement methods and differences in oxidation times (oxidation tests were only done for 24 h in [12]). Huang et al. used ASR measurements as an indirect method of calculating the activation energy, while the mass gain method used in this work is more direct and should be more reliable.

Both Y and Y/Co are potential coatings to improve the performance of fuel cell interconnects. For the same annealing temperature and duration (e.g., 750 °C and 100 h), Y/Co forms a chromia layer that is almost half the mass of that for 430 SS (Fig. 12) with a factor of seven lower resistivity. For longer oxidation times, Y- and Y/Co-coated steels have similar ASR values, with Y steels having the thinnest chromia layers. For all steels studied, there is a shift from parabolic behaviour at 800 °C, with Y/Co-coated steels showing the largest deviation. This may be an indication that the coated steels may not be suitable for temperatures exceeding 750 °C.

5. Summary

The oxidation behaviour at 700–800 °C of 430 SS, with and without sol–gel coatings, was studied. Coatings examined include Y, Co and Y/Co oxides. The results are summarized as follows:

- Two types of oxides formed for all samples studied. A continuous chromia layer (Cr_2O_3) formed adjacent to the metal substrate, while Cr–Mn spinel (approximate composition corresponding to Cr_2MnO_4) formed as a discontinuous surface layer. For Co-coated steels, the spinel layer was continuous and had a thickness comparable to the chromia layer.
- The Y-containing coatings exhibited the best oxidation resistance at all temperatures, with chromia thicknesses and mass gains less than 50% of the values for uncoated and Co-coated steel. Co-coated samples showed the worst oxidation resistance, with spinel formation greatly enhanced by the presence of Co. Oxides formed on uncoated and Co-coated stainless steels were susceptible to spalling for oxidation times in excess of 250 h.
- The Y-containing coatings had the lowest resistances (expressed as an area-specific resistance or ASR) by at least a factor of four. The low values were attributed to a combination of reduced oxide thickness (Y and Y/Co coatings) and Co doping of the chromia layer (Y/Co coatings).
- Oxidation kinetics for uncoated, Y- and Y/Co-coated stainless steels were parabolic in nature at 700 and 750 °C. At 800 °C, there was deviation from parabolic to paralinear behaviour, which was attributed to increased formation of unprotective spinel.

Acknowledgments

The authors are grateful to the Natural Sciences and Engineering Research Council (NSERC) of Canada, the Alberta Energy Research Institute (AERI) Core University Research in Sustainable Energy (COURSE) program and Versa Power Systems (VPS). VPS is also acknowledged for supplying materials and providing access to processing and testing facilities. The authors would like to thank E. Tang, A. Wood and J. Protkova of VPS for their technical and experimental assistance.

References

[1] T. Brylewski, M. Nanko, T. Maruyama, K. Przybylski, Solid State Ionics 143 (2001) 131–150.
[2] T. Brylewski, T. Maruyama, M. Nanko, K. Przybylski, J. Thermal Anal. Calorim. 55 (1999) 681–690.
[3] T. Horita, Y. Xiong, H. Kishimoto, K. Yamaji, N. Sakai, H. Yokokawa, J. Power Sources 131 (2004) 293–298.
[4] L. Mikkelsen, S. Linderoth, Mater. Sci. Eng. A 61 (2003) 198–212.
[5] H. Kurokawa, K. Kawamura, T. Maruyama, Solid State Ionics 168 (2004) 13–21.
[6] T. Horita, Y. Xiong, K. Yamaji, N. Sakai, H. Yokokawa, J. Power Sources 118 (2003) 35–43.
[7] G.V. Samsonov, The Oxide Handbook, Plenum Press, London, UK, 1973, p. 271.
[8] S. Chevalier, J.P. Larpin, Acta Mater. 50 (2002) 3107–3116.
[9] S. Chevalier, G. Bonnet, J.P. Larpin, J.C. Colson, Corros. Sci. 45 (2003) 1661–1673.
[10] N. Oishi, Y. Yamazaki, Electrochem. Soc. Proc. 99 (1999) 759–766.

[11] W.Z. Zhu, S.C. Deevi, Mater. Sci. Eng. A 348 (2003) 227–243.
[12] K. Huang, P.Y. Hou, J.B. Goodenough, Mater. Res. Bull. 36 (2001) 81–95.
[13] F. Riffard, H. Buscail, E. Caudron, R. Cueff, C. Issartel, S. Perrier, Mater. Charact. 49 (2002) 55–65.
[14] F. Riffard, H. Buscail, E. Caudron, R. Cueff, C. Issartel, S. Perrier, Appl. Surf. Sci. 199 (2002) 107–122.
[15] W. Qu, L. Jian, D.G. Ivey, J. Power Sources 138 (2004) 162–173.
[16] J. Li, Ph.D. Thesis, University of Illinois, Urbana-Champaign, Illinois, 1995, p. 41.
[17] K. Huang, P.Y. Hou, J.B. Goodenough, Solid State Ionics 129 (2000) 237–250.
[18] JADE Version 7 Software – XRD Processing, Identification and Quantification, Materials Data, Inc., 2004.
[19] Phase Equilibria Diagrams Database, National Institute of Standards and Technology, American Ceramic Society, CD-ROM Database Version 2.1, Westerville, Ohio, 1998.
[20] M.J. Cristobal, P.N. Gibson, M.F. Stroosnijder, Corros. Sci. 38 (1996) 805–822.
[21] W.C. Hagel, A.U. Seybolt, J. Electrochem. Soc. 108 (1961) 1146–1152.
[22] S.A. Bradford, Corrosion Control, CASTI Publishing Inc., Edmonton, Alberta, 2001, p. 443.
[23] R.E. Lobnig, H.P. Schmidt, K. Hennesen, H.J. Grabke, Oxid. Met. 37 (1992) 81–93.
[24] P.Y. Hou, J. Stringer, Mater. Sci. Eng. A 202 (1995) 1–10.
[25] C. Ostwald, H.J. Grabke, Corros. Sci. 46 (2004) 1113–1127.
[26] W. Qu, L. Jian, J. Hill, D.G. Ivey, J. Power Sources 153 (2006) 114–124.